九州大学学術情報リポジトリ
Kyushu University Institutional Repository

Maximising mechanical properties of aluminium alloys by microstructural optimisation using a coarsened surrogate model

Toda, Hiroyuki
Department of Mechanical Engineering, Kyushu University

Hirayama, Kyosuke
Department of Mechanical Engineering, Kyushu University

Li, Han
Department of Mechanical Engineering, Kyushu University

Batres, Rafael
Campus Cuernavaca, School of Engineering and Sciences, Tecnológico de Monterrey

他

https://hdl.handle.net/2324/7234366

出版情報：Computational Materials Science. 243, pp.113115-, 2024-07. Elsevier
バージョン：
権利関係：© 2024 The Authors.

KYUSHU UNIVERSITY

Computational Materials Science 243 (2024) 113115

Contents lists available at ScienceDirect

Computational Materials Science

journal homepage: www.elsevier.com/locate/commatsci

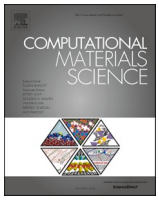

Full Length Article

Maximising mechanical properties of aluminium alloys by microstructural optimisation using a coarsened surrogate model

Hiroyuki Toda [a,*], Kyosuke Hirayama [a,d], Han Li [a,b], Rafael Batres [c], Seo Dowon [a], Hiro Fujihara [a]

[a] Department of Mechanical Engineering, Kyushu University, 744, Motooka, Nishi Ward, Fukuoka City, Fukuoka 819-0395, Japan
[b] College of Informatics, Huazhong Agricultural University, 1, Shizishan Jie, Hongshan Qu, Wuhan 430070, China
[c] Campus Cuernavaca, School of Engineering and Sciences, Tecnológico de Monterrey, Av. Eugenio Garza Sada 2501 Sur, Tecnológico, 64849 Monterrey, N.L., Mexico
[d] Department of Materials Science and Engineering, Kyoto University, Yoshida Honmachi, Sakyo-ku, Kyoto 606-8501, Japan

ARTICLE INFO

Keywords:
Micro-tomography
Particle damage
Surrogate model
Data coarsening
Finite element simulation
Image-based numerical simulation

ABSTRACT

Surrogate-based microstructural optimization was applied to describe the relationship between local microstructural patterns and particle damage in wrought 2024 aluminium alloy. A support vector machine was used to realise high-accuracy optimisation from a limited number of high-computational-cost image-based simulation results. The methodology integrated thoroughgoing microstructural quantification, a couple of coarsening processes, and surrogate modelling. The following three objective functions were defined: the maximum principal stress in particles, the equivalent plastic strain, and the stress triaxiality in the matrix. A number of design parameters were comprehensively prepared that quantitatively expressed the size, shape, and spatial distribution of particles and pre-existing micro pores in numerous ways. The number of design parameters was then reduced from 86 to 4 for each objective function during the coarsening process. The surrogate model provided the dependency of particle damage for the size, shape, and spatial distribution of particles and micro pores in the form of a multi-dimensional response surface. It has been established that micro void formation can be described using the simple volume and surface area of particles through the elevation of particle stress and the increase in equivalent plastic strain in the matrix, and the spatial distribution of pre-existing micro pores is of crucial importance for micro void growth through the elevation of stress triaxiality in the matrix. The proposed material microstructure optimisation method provides relationships between complex local microstructural patterns and material properties that are not available from existing material development approaches. It is a computationally inexpensive and reasonable method that can optimise the complex and irregular microstructures of real materials with high efficiency and accuracy.

1. Introduction

One of the ultimate goals of materials science and engineering is to find a microstructure-property relationship that describes the optimal and weakest microstructural features. Although such investigations have been experimentally performed on a trial and error basis, it is very time consuming and impossible to find the optimal microstructure in a vast multi-dimensional design space. From the commencement of research on a new material to its practical application, it typically takes a long time, 10–20 years or more [1]. The trial-and-error approach of repeating the loop of material design, prototyping and testing not only requires a long period of time, but also has the problem that precise optimisation can never be reached.

By the way, theoretical analysis based on a simplified model (e.g., irregular distribution of particles with complex morphologies simplified to a 2D quadrant with periodic boundary conditions) are usually only effective for qualitative understanding of general trends, and it is not realistic to pursue microstructural optimization in practical materials with complex microstructure [2,3]. A similar approach is the isometrical topology optimisation of periodic lattice materials [4]. Some of these utilise 2D or 3D finite elements as microstructures [5]. Such microstructures can be fabricated in practice, e.g. by employing the additive manufacturing methods [6,7]. However, this study assumes the optimisation of the microstructure of structural metals that have undergone normal manufacturing processes, such as casting and/or thermos-mechanical treatment, and does not cover the optimisation of special

* Corresponding author.
E-mail address: toda@mech.kyushu-u.ac.jp (H. Toda).

https://doi.org/10.1016/j.commatsci.2024.113115
Received 8 February 2024; Received in revised form 11 May 2024; Accepted 17 May 2024
Available online 31 May 2024
0927-0256/© 2024 The Authors. Published by Elsevier B.V. This is an open access article under the CC BY-NC license (http://creativecommons.org/licenses/by-nc/4.0/).

materials.

An alternative to the conventional modelling described above is the correspondence of various process and design variables to macroscopic material properties using the machine learning [8–10]. Data mining-based statistical modelling has been applied by employing tools such as artificial neural networks or Gaussian processes to quantify the influence of variations of input variables such as the concentrations of alloying elements on an output such as strength and ductility, provided that sufficient data which comprises the boundaries of the whole design space has been provided. An example of this application is the relationship between chemical composition and macroscopic properties in nickel-based superalloys [11–13]. With a sufficiently large number of data sets, a simple correspondence between material properties and various chemical compositions is achievable, albeit with considerable ambiguity. Furthermore, if materials are fabricated under various process conditions by varying such as temperature and time conditions and their macroscopic properties are evaluated, the optimum process conditions that maximise the macroscopic properties can be identified [14–16]. Thus, it is not difficult to simply obtain a statistical relationship between the values of various manufacturing conditions and macroscopic properties. It is however not easy to ascertain the changes in microstructure when chemical compositions, process conditions, etc. are changed and to obtain a constitutive relationship between detailed microstructural features and the macroscopic properties that can be interpreted physically. In this case, optimisation in the true sense of the term cannot be achieved unless the complex and irregular microstructure of the real materials, its variability, and complex spatial distribution can be taken into account. To the authors' knowledge, few examples of such physical optimisation have been reported. For example, Sun et al. measured the volume fraction, average thickness, etc. of the α-phase of a Ti-6Al-4V alloy and determined the relationship with the strength and ductility of 54 specimens using an artificial neural network [8]. However, only simplified microstructure-properties relationships, such as yield strength increasing with decreasing α-phase thickness, have been obtained, which can be understood within the scope of the present academic knowledge. This is far from the true microstructural optimisation described above.

Numerical simulations have also been applied to such issues. Simulation can be a powerful tool in that it can replace experiments and provide results in a short time. The simplest simulation tool is material modelling to build phenomenological constitutive models based on macroscopic experimental measurements. In this case, although modelling to account for microscopic slip and void initiation/growth is also possible, but microscopic behaviour is not modelled explicitly. If the microstructure is simplified to the limit by assuming geometrical periodicity, simulations are carried out using a combination of unit cells and periodic symmetry conditions. Numerical simulations of nano- and micro-scopic phenomena have also been widely attempted by utilising representative volume elements (RVEs) representing complex microstructures. For RVEs, virtual microstructures are used in some cases, while others accurately reflect the 3D microstructure of real materials. The attempt called integrated computational materials engineering (ICME), which combines these with databases, machine learning, etc., aims at optimising the design of structural components from material design [17,18]. However, true microstructural optimisation cannot be achieved unless the irregular and heterogeneous microstructure of real-world materials is incorporated into the optimisation. In other words, although the influence of microstructure can be qualitatively assessed, it is difficult to accurately predict the macroscopic properties and behaviour [19]. Moreover, the accuracy of those methods is not high enough to enable optimisation of the microstructure of complex and irregular practical materials. For example, Raβloff et al. investigated the relationship between pores and fatigue properties of a Ti-6Al-4V alloy by employing the 3D crystal plasticity finite element analysis, with 307 simulation executions for four models. Although they have succeeded in identifying some dominant factors, there are significant differences in trends from widely used empirical model [20].

In modern materials science, computational methods have emerged that can accurately model various material behaviours at different length scales. In particular, 3D image-based numerical simulations are becoming increasingly important, compared to the conventional numerical simulations that typically use simplified and symmetrized models or various homogenisation techniques [21,22]. In this respect, 3D imaging modalities involving synchrotron X-ray micro- and nano-tomography techniques enable the creation of high-fidelity simulation models by directly converting 3D microstructural images into fine 3D meshes for numerical simulations [23–26]. A combination of appropriate optimization methods with high-fidelity 3D image-based numerical simulations provides a systematic means for designing heterogeneous micro- and nano-structures with tailored macroscopic material responses. However, employing high-fidelity simulation models for microstructural optimization in practical materials is restrictive because optimization commonly requires large numbers of trials with many different large-scale models. Computation of a high-fidelity 3D simulation model is time-consuming and, therefore, computationally expensive [27,28]. The preparation of high-fidelity 3D image-based numerical models is also extremely time consuming due to mesh clean-ups, stitching, and debugging [29], which makes the numerical simulations computationally expensive. For example, the creation of the image-based computer models in this study took approximately one week per model. Finally, the creation of all 15 models took almost three months. It is clear that if a similar result were to be achieved simply by increasing the number of analysis models rather than the surrogate model analysis used in this study, it would take an unrealistically long time.

The authors propose a methodology for optimizing the mechanical properties of structural metals by integrating a limited number of high-fidelity 3D image-based numerical simulations, their high-fidelity quantification and subsequent coarsening (i.e., a reduction in the number of microstructural design parameters), and the final optimisation with surrogate modelling [30]. The need for the coarsening process is to reduce the number of design variables to the extent that the accuracy of the analysis is not compromised by coarsening, which ensures industrial accessibility by reducing the number of design variables to be used for material design. It is also linked to evaluation in three dimensions or less so that the engineers (i.e., evaluator) can intuitively understand and make decisions, saving computational resources by shortening surrogate model calculation. In the proposed methodology [30], the support vector machine [31,32] was used with an infill sampling criterion [33], which effectively alleviated the computational burden by reducing the number of numerical trials needed to find the final solution.

In the previous study, the effectiveness of the proposed technique was demonstrated and validated for optimising the size, shape, and spatial distribution of irregularly shaped Al_2Cu particles that coexist with microscopic pores in wrought 2024 aluminium alloy [30]. A strategy to address the issue of microstructural optimisation in such particulate materials would be direct optimisation of the size and morphology with respect to individual particles. However, this would not be the most efficient approach if particle clusters or interactions among neighbouring particles are of crucial importance. In fact, in the previous research, most of the design parameters associated with particle spatial distributions did not survive the coarsening processes, and the sole surviving design parameter on spatial distribution exhibited a relatively low correlation coefficient with the objective function on damage [30], which is contrary to the expectation that particle clustering is detrimental [34]. *k*-nearest neighbour's algorithm and *k*-means clustering were employed to define average distance and local volume fraction values in each cluster to express particle clustering, which was then assigned to all particles that belonged to clusters [30]. However, this was not the most efficient approach because it was apparent that all the particles that belonged to a particle cluster were never equally

damaged. It was, therefore, inferred that particle spatial distribution and interaction effects should be more adequately considered.

To solve the particle clustering problem, it was assumed in the present study that the macroscopic strength of a particulate material originated from the in-situ strength of the weakest region of an appropriate finite size. Also, to fully capture the statistical nature of local damage events, normally a large number of data points (the computational results) are needed to fill the design space. To reduce the number of computational models needed, optimization was carried out by combining a surrogate-based algorithm with an in-fill sampling criterion that had been constructed in the previous study [30]. The correlation between microstructural parameters and particle damage was evaluated comparatively with the single-particle optimization in the previous study.

2. Methods for image-based finite element simulations and surrogate-based optimisation

2.1. 3D modelling processes for finite element simulations

The methodology for the surrogate-based optimization used in this study is summarized in Fig. S1. We performed an image-based numerical simulation with high-fidelity 3D models of the irregular and complex microstructures in Step 2 after capturing high-fidelity 3D images in Step 1.

Wrought 2024 aluminium alloy was assumed as the model material. The alloy contained irregularly shaped coarse Al_2Cu particles and microscopic pores that were nucleated heterogeneously on Al_2Cu particles, as shown in Fig. 1. The micro pores had an average diameter of 2.3 μm, a number density of 134,000/mm^3, and a volume fraction of 0.28 %. Al_2Cu particles had an average diameter of 3.8 μm, a number density of 620,000/mm^3, and a volume fraction of 3.9 % [35]. The details of the material are available elsewhere (Material HH of ref. [35]). A high-resolution 3D tomographic image of substantial spatial resolution of 1.0 μm from past research was used, as was the case in the previous paper [30]. The whole field of view was approximately 600 × 600 × 600 μm. It is crucially important that the microstructural features to be analysed are captured with sufficient accuracy and fields of view. And in regard to the damage from the particles and micro pores of the material used, this condition was met.

For the first step, we randomly selected the regions of interest (regular cubes of 40 × 40 × 40 μm) for 3D image-based numerical models from the whole field of view, as shown in Fig. 1. The size of the unit box was determined so that a few particle clusters could easily fit inside it. The microstructural design parameters, which will be described later, were expected to reasonably cover a multi-dimensional space that was feasible. STL meshes of particles and micro pore surfaces were obtained after volume rendering and then divided into 3D using tetrahedral elements (Fig. 1). In total, ten unit boxes (Region 6–15 in Fig. 3) were randomly selected from 360,000 possible microstructural patterns that were sampled by translating a regular cube unit box by 10 μm in all the *x*, *y*, and *z* directions in the 3D image. Some of the examples are shown in Fig. 2 (b)–(f); they correspond to Region 6–10 in Fig. 3. In order to predict the optimal or weakest microstructural pattern that could be located outside that of the practical material used for modelling, the microstructural design parameters should fundamentally be spread beyond the experimental data dispersion obtained from a specific real-world practical material in the design space. Fig. 2 (a) is of the region where the number density and volume fraction values of Al_2Cu particles and micro pores are the closest to their average values in the whole field

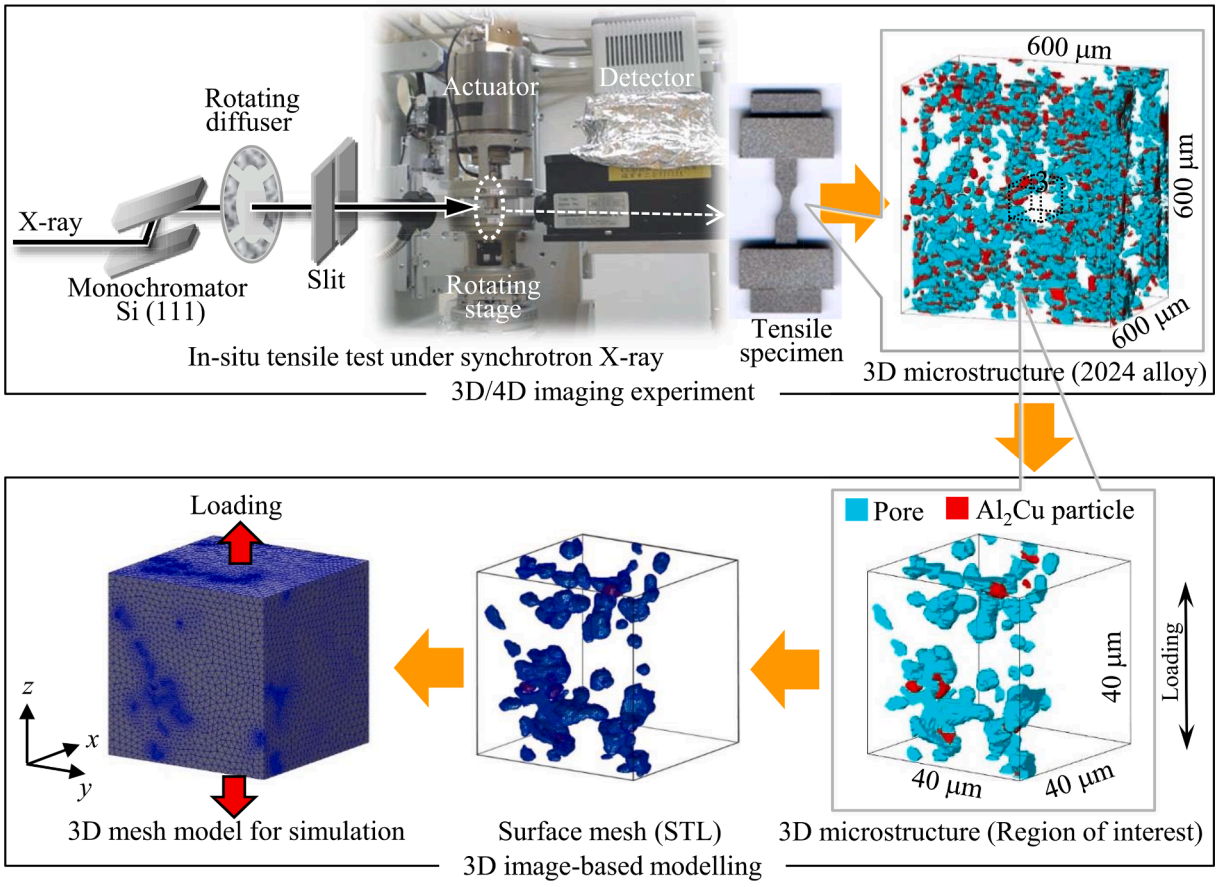

Fig. 1. This is a schematic illustration of preliminary 3D/4D imaging of a material test in a synchrotron radiation facility and subsequent preparation of a 3D image-based simulation model.

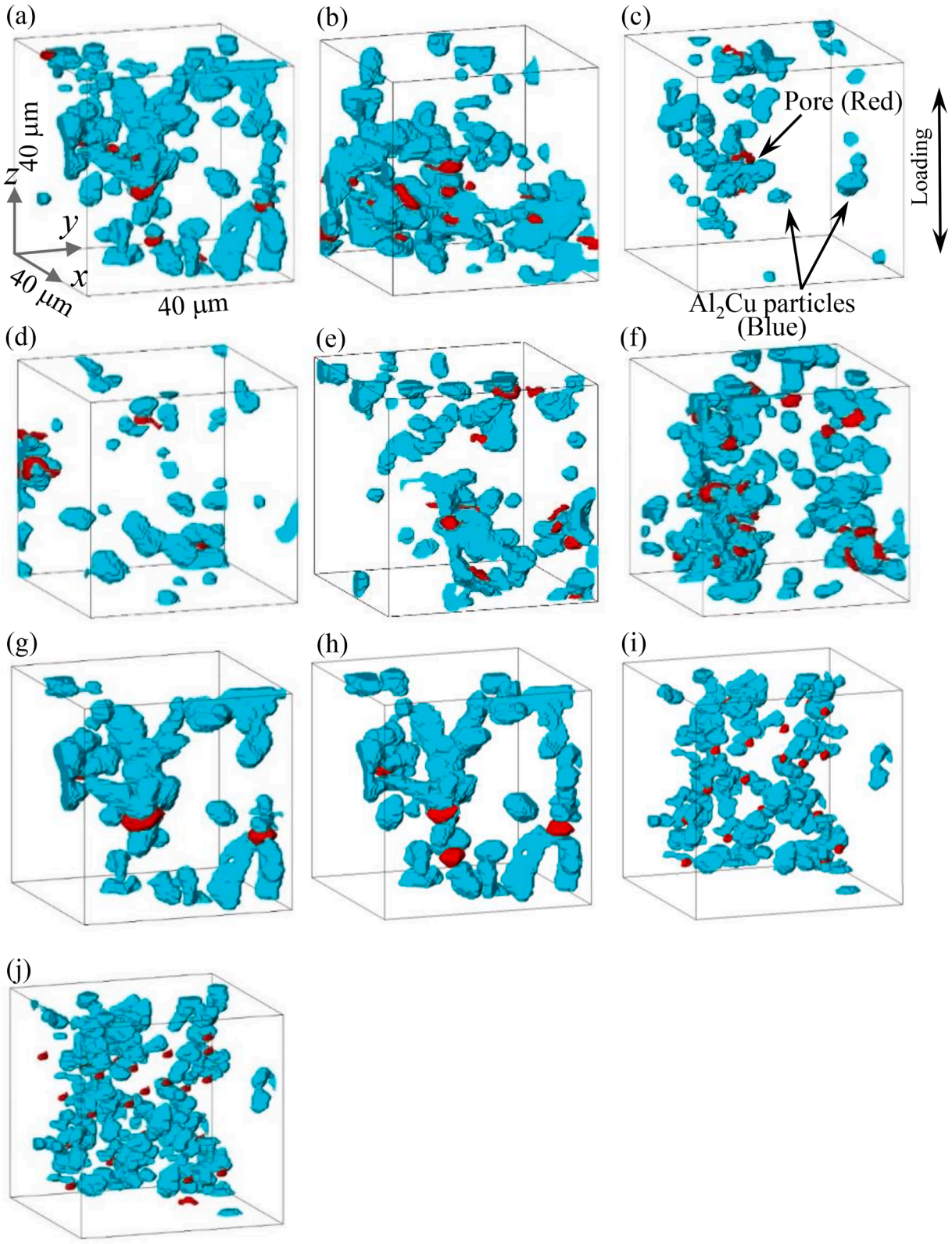

Fig. 2. (b)–(f) are 3D views of the five local regions (Region 6–10 in Figs. 4 and 5) that were used in the 3D image-based numerical simulation. Only micro pores and Al_2Cu particles are displayed, which are represented in red and light blue, respectively. The underlying aluminium is not displayed. A regular hexahedron-shaped unit box with the dimensions $40 \times 40 \times 40$ μm^3 was randomly sampled in the whole field of view of the X-ray micro-tomography image, as shown in Fig. 1. Five of the fifteen microstructural patterns are shown here. (a) is the region where the number density and volume fraction values of both Al_2Cu particles and micro pores are the closest to the average values for the whole field of view (number densities of 1.34×10^{14} and 6.20×10^{14} / m^2 and volume fractions of 0.28 and 3.9 % for micro pores and particles, respectively). (a) was used as Region 5, as shown in Figs. 3 and 5. (For interpretation of the references to colour in this figure legend, the reader is referred to the web version of this article.)

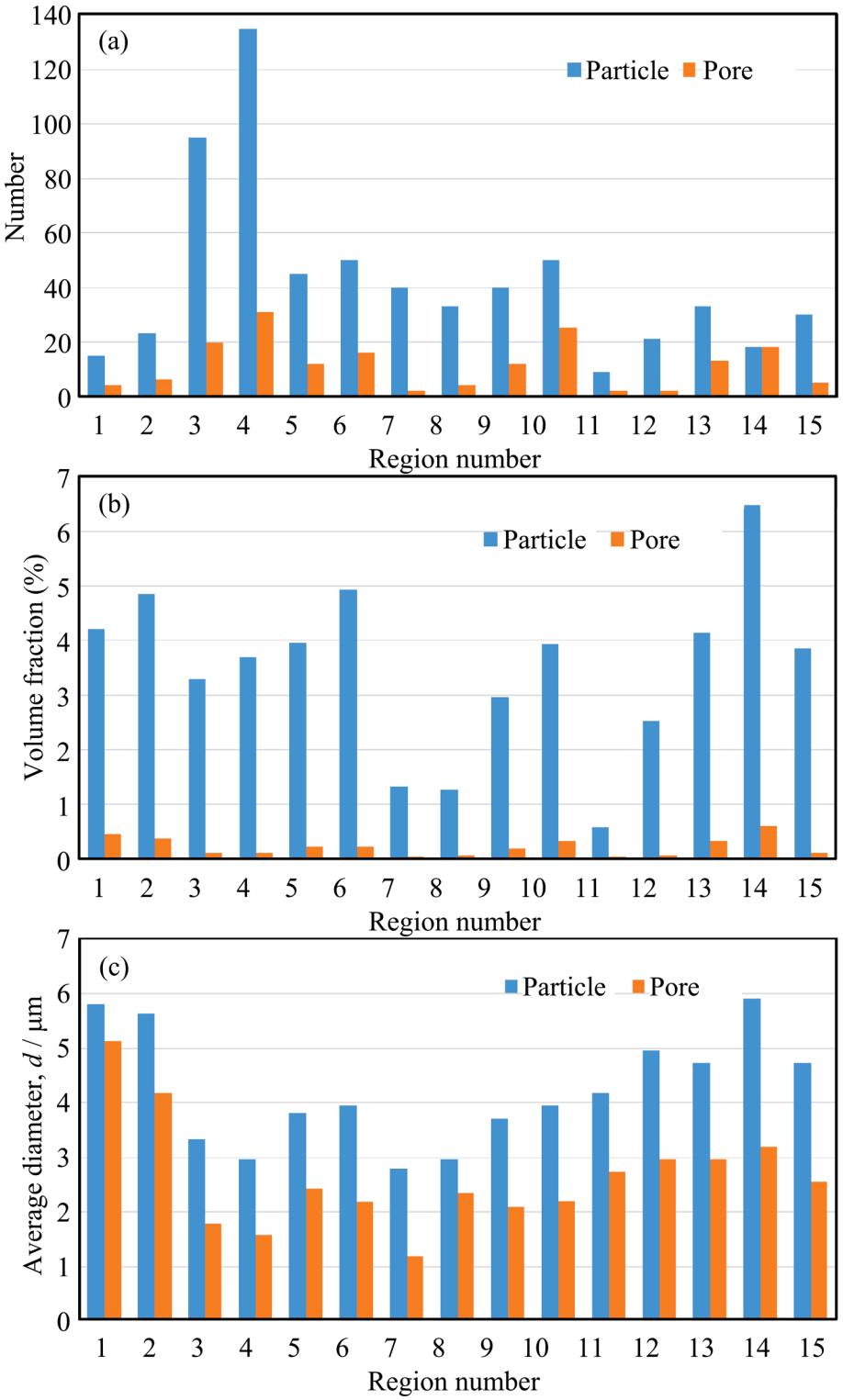

Fig. 3. This shows the number, volume fraction, and average size of Al_2Cu particles and micro pores for all the fifteen selected 3D microstructural patterns used for preparing 3D image-based simulation models and the quantities for the unit boxes (regular hexahedrons of 40 × 40 × 40 μm^3).

of view. It is shown as Region 5 in Fig. 3. Particles and micro pores can be intentionally copied or eliminated from Region 5 in order to change microstructural patterns beyond that of the model material used. Features that were eliminated were randomly selected. Intentionally added features were randomly selected and then randomly located and rotated. For Region 1–4 (Fig. 3), the density values of both particles and micro pores were made one third, halved, doubled, or tripled compared to Region 5. Fig. 3 summarizes the number, volume fraction, and average diameter of micro pores and particles in all of the fifteen models prepared. Local areas of 40 μm square containing particles and pores more than three times the average were actually present between the points of the samples used with a probability of 1.7 % and 5.8 % respectively. On the other hand, regions containing less than 1/3 of the average also existed with a probability of 11.6 % and 31.9 % for particles and pores

respectively. It can therefore be seen that models with artificially increased or decreased particles and pores do not deviate from the real design space. The numbers of tetrahedral elements and nodes for Region 5 in Fig. 2 (a) are 89,803 and 133,319, respectively, and those for the other models ranged within ± 5 % of those values.

2.2. Image-based finite element simulations

The Al_2Cu particles and the aluminium matrix were assumed to be elastic and elasto-plastic, respectively. Young's moduli of the particles and the matrix were assumed to be 69.0 and 105 GPa, respectively, and the Poisson ratios 0.33 and 0.34, respectively [36]. The elastic–plastic response of the 2024 aluminium was assumed to follow a stress–strain curve [37].

The commercial finite element simulation software Marc/Mentat was used to obtain stress/strain distributions in the 3D image-based numerical models. A uni-axial tensile strain of 5 % was applied between the upper and lower surface planes of the 3D image-based numerical models. Additional details about the computations are available [37].

An example of the finite element simulation results as the distributions of equivalent plastic strain on the whole and two magnified specific cross-sections of Region 5 is shown in Fig. 4. Plastic strain accumulation was especially observed in the vicinity of Al_2Cu particles around particle corners, as shown in Fig. 4 (b), together with internal stress elevation inside Al_2Cu particles. Micro pores also accelerated the matrix flow, as shown in Fig. 4 (c), thereby promoting the strain accumulation around Al_2Cu particles. The distributions of equivalent plastic strain, normal stress, and stress triaxiality were utilized to calculate three objective functions, as described in section 2.4. While the normal stress and stress triaxiality data were not obtained from the X-ray CT (hereafter XCT) experiments, the plastic strain data was. As was demonstrated in the companion paper [30], significant local variations in the three mechanical quantities were observed (Figs. 3 and S2 [30]), especially where coarse Al_2Cu particles were irregularly shaped.

2.3. Design parameters for surrogate-based optimization

Initially, the quantification of microstructural features, such as size, shape, and spatial distribution, was performed by utilizing a considerable number of design parameters, as shown in Step 3 of Fig. S1. All the design parameters used for quantification are listed in Table S1. A variety of morphological parameters were prepared to describe the shapes of particles and pores involving morphological complexity, such as orientation, aspect ratio, deviations from cube or sphere, connectivity, and surface complexity. Multiple parameters were also prepared to describe size and spatial distribution. The total number of design parameters was initially 43 for both particles and micro pores (9 parameters for size, 24 for shape, and 10 for spatial distribution). Design parameters for size and shape were identical to those used in the companion paper, where the size, shape, and spatial distribution of individual particles were optimized [30].

In terms of size measurements, D expresses the volume equivalent to spherical diameter. V and S represent the volume and surface area that were measured after applying the Marching Cubes algorithm. L, W, and T were measured by creating the smallest rectangular bounding box that completely surrounded a micro pore or a particle, and they correspond to x ,y, and z in the global Cartesian coordinate system, respectively. In addition, B simply denotes the volume of the bounding box ($B = L \times W \times T$). Finally, G describes the so-called geodesic distances, which are the shortest continuous surface paths between the uppermost and lowermost points of the particles or pores.

In terms of shape, $f^1 - f^{10}$ were calculated using L, W, T, V, S, and M, where M denotes the convexity properties obtained as the integral of the mean curvature of a particle or pore. The equations for calculating $f^1 - f^{10}$ are listed in Table S1 [29]. $f^1 - f^3$ stand for aspect ratios. $o^4 - o^6$ also stand for aspect ratios measured along the three principal axes. f^{10} is also an index for particle/pore elongation. f^4 and f^8 / f^9 measure the deviations from the spherical and cubic shape of a particle or pore, respectively. $f^5 - f^7$ stand for convexity properties. Similarly, C and E denote the mean curvature of an object and the Euler number, which describe the surface complexity and connectivity, respectively [29]. θ expresses the angle between the loading direction and the first principal axis [29].

The 3D version of moment invariants, which were first introduced by Sadjadi and Hall, were also used for describing the morphological features of the particles and pores [29,38]. The first moment invariants, p^2, p^3, and p^4, define the central locations along the x ,y, and z directions, respectively. The second moment invariants, p^5, p^6, and p^7, represent the deviation from the centre and describe the degree of spread in the voxel distribution. The third moment invariant, p^8, defines skewness, which is a measure of the distortion of the voxel distribution. The fourth moment invariant, p^9, defines kurtosis as a measure of tailedness. A 3D object can be described by the grey value distribution function, $f(x, y, z)$. For a binary image, $f(x, y, z) = 1$ represents internal voxels that belong to an object and $f(x, y, z) = 0$ when they are outside an object. The 3D moments of order n ($=p + q + r$), m_{pqr} are defined for $p, q, r = 0, 1, 2\ldots$ as $m_{pqr} = \sum_x \sum_y \sum_x x^p y^q z^r f(x, y, z)$. For $n = 1$ (the first-order moment invariants), $p_2 = m_{100}/m_{000}$ is along the x axis, $p_3 = m_{010}/m_{000}$ along the y axis, and $p_4 = m_{001}/m_{000}$ along the z axis. For $n = 2$ (the second-order moment invariants), $p_5 = (m_{200} + m_{020} + m_{002})/m_{000}^{5/3}$, $p_6 = (m_{200}^2 + m_{020}^2 + m_{002}^2 + 2m_{110}^2 + 2m_{101}^2 + 2m_{011}^2)/m_{000}^{10/3}$, and $p_7 = (m_{200}{*}m_{020}{*}m_{002} - m_{002}{*}m_{110}^2 - m_{020}{*}m_{101}^2 - m_{200}{*}m_{011}^2 + 2{*}m_{100}{*}m_{101}{*}m_{011})/m_{000}^4$.

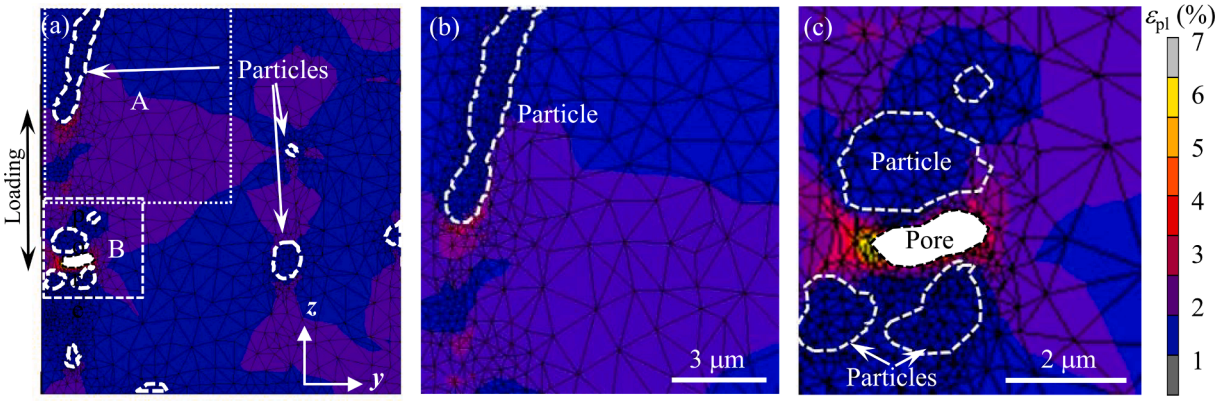

Fig. 4. This shows the magnified views of the output of the finite element analysis displayed on y-z virtual cross-sections. (a) is a part of the whole cross-section. (b) and (c) are enlarged views of A and B in (a), which show the strain distribution around the elongated Al_2Cu particle and the particle cluster, respectively.

For $n = 3$, $p_8 = \left(m_{300}^2 + m_{030}^2 + m_{003}^2 + 3m_{120}^2 + 3m_{102}^2 + 3m_{012}^2 + 3m_{021}^2 + 3m_{210}^2 + 3m_{210}^2 + 6m_{111}^2\right)/m_{000}^5$. For $n = 4$, $p_9 = (m_{400} + m_{040} + m_{004} + 2m_{220} + 2m_{202} + 2m_{022})/m_{000}^3$. All of the moment invariants are invariant under translation and changes in scale and rotation.

The majority of the design parameters for quantifying spatial distribution were not the same as those used in the companion paper [30]. In that paper, the spatial distribution of individual particles was optimized by utilizing the k − nearest neighbourhood algorithm, with K meaning the clustering algorithm [30]. And the average distance and local volume fraction values within a cluster in which the particle of interest was embedded were assigned to the particle concerned. However, in this study, spatial distribution patterns were quantified for each unit box. The k − nearest neighbourhood algorithm [29,39] was also utilized for $k = 2$, 3, and 5. The density for each unit box was simply defined as N / V, where N is the number of particles or pores in a unit box. G-function, G, is a cumulative nearest-neighbour function that measures the fraction of nearest-neighbour distances that are less than or equal to the distance t, as $G = \frac{1}{N}\sum_{i=1}^{N} I(y_i \le t)$, where y_i is the distance of cell i to its nearest neighbour [29,40]. F-function, F, is similar to G-function except that the distance from each grid point, which was placed at regular intervals throughout the sample field, to its nearest neighbour cell was measured [29,41]. So $F = \frac{1}{g}\sum_{i=1}^{g} I(y_i \le t)$, where y_i is the distance of grid point i to the nearest cell. Spatial auto-correlation was also defined to measure the spatial dependence between data observed at different locations across the space. Global spatial auto-correlation, *Global*, is defined as $Global = \sum_{i=1}^{N}\sum_{j=1}^{N} a_{ij}(x_i - \overline{x})(x_j - \overline{x}) / (S^2 \sum_{i=1}^{N}\sum_{j=1}^{N} a_{ij})$, where $S^2 = \frac{1}{N}\sum_{i=1}^{N}(x_i - \overline{x})^2$, x_i is the ith observed micro pore, and $\overline{x} = \frac{1}{N}\sum_{i=1}^{N} x_i$ is the average of x_i [42]. a_{ij} is the adjacency criterion defined as $a_{ij} = 1$ if location x_i is adjacent to location x_j, and $a_{ij} = 0$ if x_i is not adjacent to x_j. Geary's C is based on the weighted sum of the square difference among objects, which is defined as $Geary = \frac{N}{2\sum_{i=1}^{N}\sum_{j=1}^{N} a_{ij}} \frac{\sum_{i=1}^{N}\sum_{j=1}^{N} a_{ij}(x_i - x_j)^2}{\sum_{i=1}^{N}(x_i - \overline{x})^2}$ [43]. Moran's I is expressed similarly as $Moran = \frac{N}{2\sum_{i=1}^{N}\sum_{j=1}^{N} a_{ij}} \frac{\sum_{i=1}^{N}\sum_{j=1}^{N} a_{ij}(x_i - \overline{x})(x_j - \overline{x})}{\sum_{i=1}^{N}(x_i - \overline{x})^2}$ [44]. Getis's global, *Getis*, is defined by $Getis = \sum_{i=1}^{N}\sum_{j=1}^{N} a_{ij}(t) x_i x_j / \sum_{i=1}^{N}\sum_{j=1}^{N} x_i x_j$ [45].

Although it seems to be excessive to express the morphological features of particles and micro pores, the majority of the design parameters with lower degrees of correlation were screened out later in the coarsening process. A sufficient number of design parameters must be prepared so that a limited number of selected design parameters can accurately express the global trends of microstructure-property relationships. In addition, a sufficient number of 3D image-based numerical models must be prepared so that the design parameters cover a design space that is feasible for capturing the global trends of data dispersion. Fig. 3 shows that this has been realized in this study for particle and pore size and density. All the design parameters were normalized to be between 0 and unity so that there was a 99 % confidence interval for the frequency distribution in each parameter having unity, as demonstrated in Fig. S3 of the companion paper [30].

2.4. Objective functions for surrogate-based optimization

Some objective functions were defined so that the contributions of particles and pores on ductile fractures were expressed as independent mathematical parameters. In this study, three objective functions, I_1, I_2, and I_3, were defined in order to evaluate the damage initiation and early growth of particles, which are the sensitive indicators of fracture resistance for the onset of ductile fractures in aluminium alloy [30]. I_1 I_2, and I_3 express the volume fractions of the regions in the unit boxes, where the maximum principal stress in Al_2Cu particles, the equivalent plastic strain of the matrix aluminium in the vicinity of Al_2Cu particles, and the stress triaxiality of the matrix in the vicinity of Al_2Cu particles exceed their critical values, respectively. Actual critical values were set to be 1000 MPa, 0.05, and 1.1 for I_1 I_2, and I_3, respectively. It is reasonable to assume that internal stress increases inside Al_2Cu particles where plastic strain is localized in the underlying matrix, which then causes particle fractures or interfacial debonding. I_1 and I_2 are, therefore, associated with the micro void formation process, whereas I_3 is associated with micro void growth; high stress triaxiality causes the lateral expansion of micro voids [46]. Prior to the coarsening processes, all the objective functions and design parameters were normalized. The values of I_1, I_2, and I_3 that were obtained after the execution of the 3D image-based numerical simulations for the fifteen models are shown in Fig. 5. Although I_1 and I_2 were associated with micro void formation from Al_2Cu particles, the magnitude relationship between high I_1 models (Region 1, 5, and 14) and very low I_1 models (Region 3, 4, 8, 10, and 11) did not necessarily coincide with that for I_2; I_2 values for very low I_1 models varied widely between 0.02 and 0.22, and it seems there were more regions that were intermediate in I_2 and between the two extremes than for I_1. The regions that were susceptible to premature damage (Region 1, 5, 6, 14, and 15), which were predicted from I_1 and I_2, sometimes exhibited high I_3 values (Region 5 and 14), while Region 15 exhibited very low I_3 values (0.00012). This implies that micro void formation and growth are caused by different mechanisms, i.e., the increase and decrease in plastic deformation for micro void formation and growth, respectively. It is also noteworthy that stress triaxiality distribution may drastically change after micro void formation. Therefore, it can be assumed that I_3 values obtained from 3D image-based numerical simulations that did not consider damage nucleation and evolution, such as those performed in this study, are effective only for the very early stage of micro void growth.

2.5. Surrogate-based optimization

A combination of principal component analysis (hereinafter PCA) and global sensitivity analysis (hereinafter GSA) was applied to reduce the number of design parameters in Step 4, from which subsequent optimisation was performed effectively in Step 5, as shown in Fig. S1. PCA and GSA were utilized for eliminating similarities in the set design parameters and selecting important design parameters that had a high degree of correlation with $I_1 - I_3$, respectively.

PCA is a popular linear dimensional reduction technique for data mining. Two or more design parameters that are close to each other form a small angle on a loading chart. The set of design parameters that is closer than a pre-determined threshold angle (i.e. 5°) is eliminated leaving the design parameter with the longest distance from the origin having the strongest contribution.

GSA is a technique for apportioning the uncertainty in objective functions to the uncertainty in each design parameter. GSA is applied for selecting a limited number of design parameters with high Pearson correlation coefficients after the number of design parameters is reduced in the first step by applying PCA. The Pearson correlation coefficient quantifies the effect of the parameters on the model. In this method, variables with large Pearson correlation values are considered more significant than those yielding small values. Values greater than 0.5 generally indicate significant correlations. However, parameters with Pearson correlation values less than 0.5 can be analysed for possible confounding factors.

The details of the coarsening process are described elsewhere [30].

For popular surrogate model algorithms, the support vector machine can be effectively utilized for high dimensional data sets with a limited number of sampling data sets [31]. In this study, a support vector machine algorithm with an infill sampling criterion was introduced in Step 5 (Fig. S2), which effectively alleviated the computational burden by reducing the number of 3D image-based numerical models required to find the solution with a high degree of reliability.

Surrogate models are built using data drawn from expensive models (image-based finite element simulations) that are able to predict the

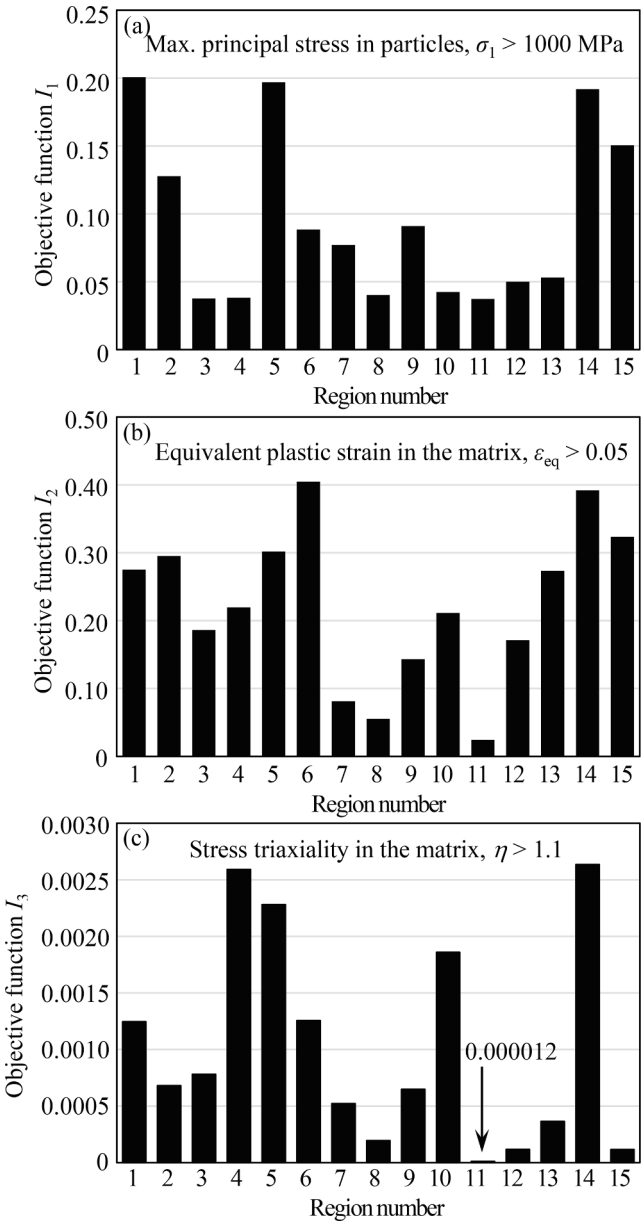

Fig. 5. This shows the three objective functions for all the fifteen regions, which were obtained by employing the 3D image-based numerical simulation. I_1 expresses the volume fraction of the regions in the unit boxes where the maximum principal stress exceeds the critical value in particles. I_2 and I_3 are the volume fractions of the regions in the unit boxes where the equivalent plastic strain (I_2) and stress triaxiality (I_3) exceed the critical values in the matrix. In essence, I_1 and I_2 / I_3 express how Al_2Cu particles and the matrix are susceptible to damage, respectively. With respect to the fracture process, I_1 / I_2 and I_3 are associated with micro void formation and growth, respectively.

output at untried points in a design space. The support vector machine can effectively handle extremely high-dimensional data from a relatively small amount of sampling data [16], outperforming compared with other optimisation methods (e.g., artificial neural networks), resulting in significant reductions in computational costs. The support vector machines were constructed using the libsvm-mat-3.25–1 Toolbox. In the proposed framework, the two common kernels (i.e., polynomial and Gaussian radial basis function) were used. In this paper, the support vector machine was used with the infill sampling criterion, which effectively alleviates computational burdens by further reducing the number of numerical trials needed to find the final solution.

In order to roughly evaluate the output from the surrogate models, response surface methodology [47] was used to explore the relationships between each objective function and a set of explanatory design parameters that had survived the coarsening process. The remaining design parameters that had not been selected for drawing a response surface were kept constant at their average values.

3. Coarsening and optimisation results

3.1. Coarsening results

The number of design parameters was reduced from 86 (43 each for both particles and micro pores) to 56 through the PCA process (Step 4 of Fig. S1). Fig. 6 shows loading charts plotted after all the 86 design parameters were categorized according to design parameter type. Parameter symbols with or without subscript “o” stand for design parameters for micro pores and Al_2Cu particles, respectively. Fig. 7 shows the top ten design parameters for each objective function. Overall, 40 % (12 of the 30 design parameters shown) of the remaining design parameters were associated with micro pores. A high percentage of the design parameters that denote particle size and shape survived (44.4 and 29.2 %, respectively), but only 10 % of the design parameters for particle spatial distribution did. On the other hand, only a low percentage of the design parameters that denote micro pore size and shape survived (11.1 and 16.7 %, respectively), but half of the design parameters for pore spatial distribution did. It is interesting to note that almost no design parameters that describe spatial distribution survived in the companion paper, where individual particle morphology was optimised [30]. However, in this study, micro pore clustering very strongly affected I_2 and I_3 even more so when local microstructural patterns in a unit box were optimised.

In general, the Pearson correlation coefficient r ranges between −1 and + 1, with positive values indicating positive relationships and vice versa. According to Evans, the strength of correlation is strong for r with values over 0.60 [48]. In the companion paper [30], r values ranged between 0.49 and 0.58, 0.32–0.41, and 0.20– 0.34 for the top four design parameters for I_1, I_2, and I_3, respectively. According to Evans’ definition, this corresponds to a weak to moderate correlation. The reason why there was considerably stronger correlation in this study is the importance of local microstructural patterns that express particle/particle interaction, particle/pore interaction, and the effects of particle/pore clustering. It can be concluded that the optimisation methodology adopted in this study for the aluminium alloy used is more reasonable than the individual particle optimisation of the previous study [30].

If the objective functions are compared, I_1 and I_2 (especially I_1) were relatively high on average, while I_3 was comparatively low. This was probably because I_1 expresses the direct criterion for micro void formation through the maximum principal stress in particles, whereas I_3 is a rather indirect criterion for void growth through the stress triaxiality of the matrix. I_2 was intermediate in its level of relevancy and correlation.

3.2. Optimisation results

The top four design parameters were selected for each objective function: (V, S, B, C), ($Getis_o$, V, S, f_o^2), ($Density_o$, $Global_o$, $Getis_o$, $Geary_o$) were selected for I_1, I_2, and I_3, respectively, as the sets of input design parameters for surrogate modelling, as shown in Step 5 Fig. S1. For all the objective functions, the values at the optimum pattern were almost zero, as can be read from Fig. 8 for I_2. It has been verified that limiting the number of design variables hardly changes the resulting surrogate model. For example, this is illustrated by increasing the number of design variables from four to five, resulting in the locations of the weakest and optimum microstructures almost identical. Due to space limitations, only the results for I_2 are shown hereafter. Comparison of the surrogate model and input computational results in this study shows

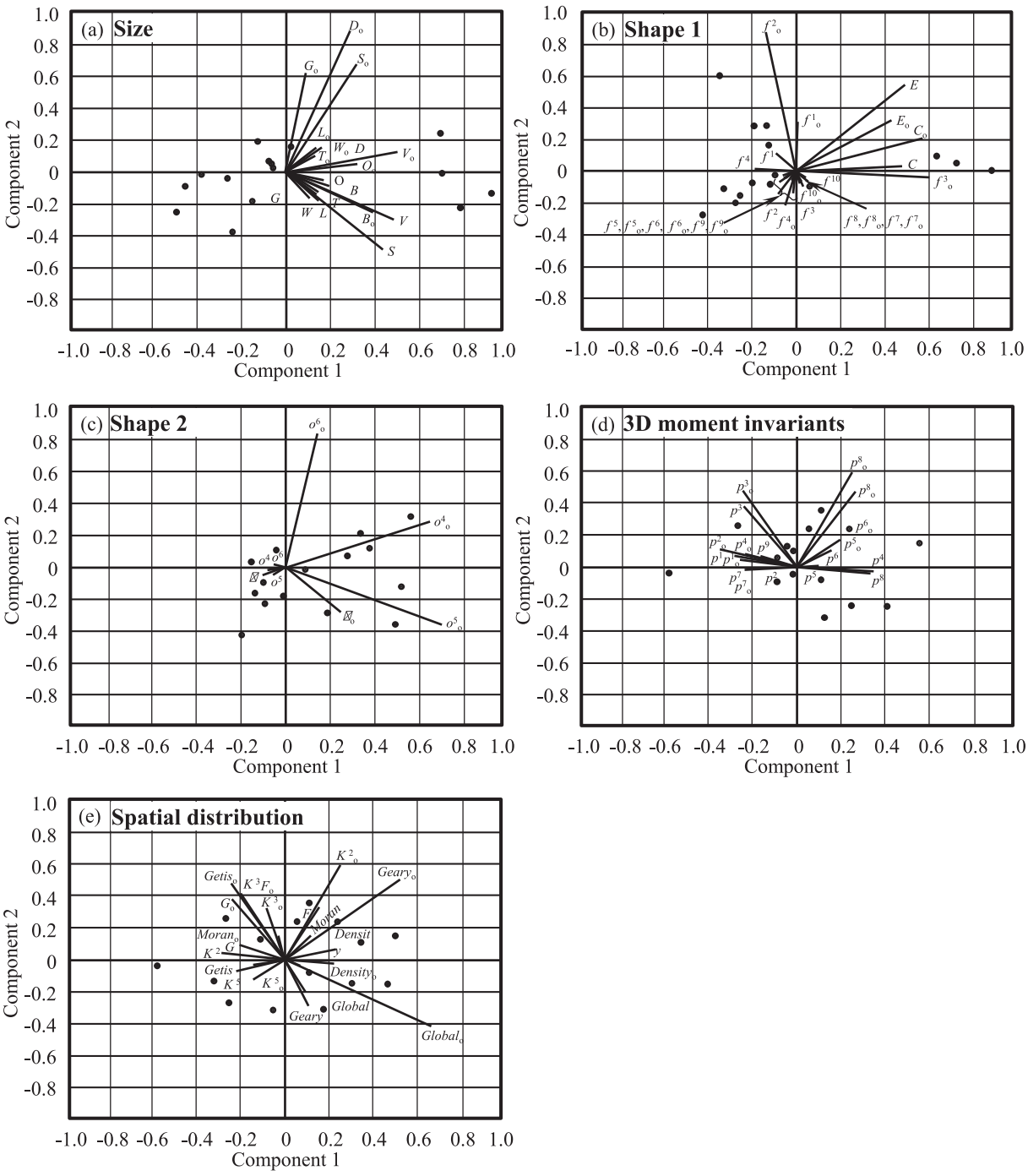

Fig. 6. This shows the principal component score distributions for every morphological category obtained by applying the principal component analysis technique. Parameter symbols with or without subscript "o" stand for design parameters for micro pores and Al_2Cu particles, respectively.

relatively good agreement, with an average of 0.58 in the surrogate model and 0.55 in the numerical results for I_2.

The 3D contour maps of the objective function I_2 were illustrated using the surrogate model. Two of the four selected design parameters were used to illustrate 3D response surface curves, as shown in Fig. 8, and the remaining parameters were fixed at their average values. The optimal (highlighted in blue) and weakest (highlighted in red) microstructural patterns are indicated by arrows in Fig. 8. The response surface exhibited the minima, where V and S were rather close to their minimum values, as shown in Table 1. The V value of 32.9 μm^3 corresponded to the equivalent spherical diameter of 2.5 μm, and sphericity, which is usually expressed as $\frac{\pi^{1/3}(6V)^{2/3}}{S}$, was 0.81. This implies that the particles in the optimised unit cell were relatively small and exhibited rather simplified shapes. The reason why very small, perfectly spherical particles are not optimal in Fig. 8 is probably because the spatial resolution of the imaging experiments used in this study is 1 μm, which is relatively close to the optimal level predicted in the analysis. The f^2_o value of 1.01 implies that the pores were not so elongated, and the $Getis_o$ value of 0.278 implies that the micro pores exhibited rather moderate dispersion (i.e., not so uniform but also not so clustered). Of all the 360,000 possible microstructural patterns that were sampled by translating the regular cube unit box by 10 μm in the x ,y, and z directions in the 3D image, the unit cell that had the closest values in $Getis_o$, V, S, and f^2_o was selected, as shown in Fig. 9.

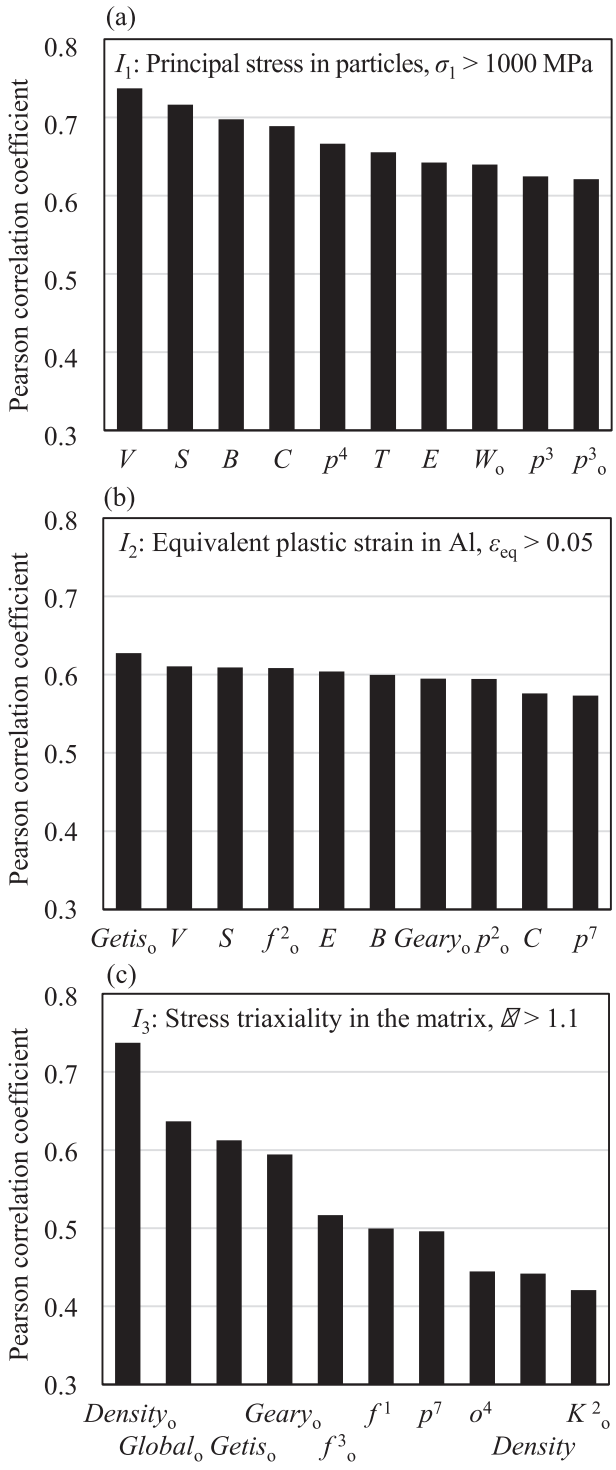

Fig. 7. This shows the results of the global sensitivity analysis, which represent the top ten design parameters with high Pearson correlation coefficients for each objective function.

In the previous study, the only design parameter associated with particle spatial distribution that survived was d_m (the average distance within each cluster based on the K means method), which exhibited a low correlation coefficient (0.26 at the maximum) [30] that was contrary to the expectation that particle clustering is detrimental [49]. It was concluded in the previous study that weak particles were identified to be coarse and probably did not cluster due to the size range of clustered particles and the relatively low internal stress in clustered particles because of the effects of interaction [30]. This may be mostly correct because design parameters associated with particle clustering disappeared (Fig. 7). The only parameter that survived was *Density*, which had a relatively low Pearson correlation coefficient (0.44). It is also noteworthy that of the 12 design parameters that survived to describe the three objective functions, half were associated with micro pores, and of these, five were associated with the spatial distribution of micro pores. This implies the importance of pre-existing micro pores for enhancing matrix plastic deformation and the elevation of stress triaxiality in the matrix.

Aluminium manufacturers can control the mechanical properties of 2024 aluminium alloy so that there are as many local regions as possible that have four design parameter values that are close to these values or, alternatively, that the weak microstructural patterns are eliminated as much as possible. It seems that the latter strategy is more realistic and efficient. High-resolution 3D tomographic imaging of 1.0 μm in substantial spatial resolution is necessary to utilise the achievements of this study. Nowadays, high-throughput production XCT systems are available for inspecting the microstructural features of structural materials in addition to the apparatus in laboratories and synchrotron radiation facilities [29,34,50]. Interestingly, the results of the analysis show that microstructural patterns with homogeneous particle and pore distributions were not necessarily the strongest. This means that design parameters have mutual dependency and cannot vary by fixing the other parameters to be constant. For example, clustered particles are sometimes small and rather spherical, whereas sparsely dispersed particles are sometimes coarse and irregularly shaped.

The relationships between the complex local microstructural patterns and material properties obtained with the present approach are not available with existing material development approaches. This not only enables highly efficient and accurate optimisation of the complex and irregular microstructures of real materials, but also leads to seemingly unexpected and unanticipated discoveries, as described above, that could lead to dramatic improvements.

A series of the techniques have been successfully applied to a range of materials engineering problems such as the characterisation of surface grain properties leading to intergranular hydrogen embrittlement cracking in 7000 series alloys, the characterisation of surface grain properties leading to fatigue crack initiation in titanium alloys and the characterisation of grain damage in aluminium due to hydrogen embrittlement [50–52].

4. Conclusion

The surrogate-based microstructural optimization of structural metals was applied to describe the relationship between local microstructural features and particle damage in wrought 2024 aluminium alloy with dispersed particles and micro pores. The support vector machine was used with an infill sampling criterion for optimisation and was highly effective in analysing the limited number of data sets (the results of a 3D image-based numerical simulation). The methodology integrated thoroughgoing microstructural quantification, a couple of coarsening processes, and surrogate modelling. The study was intended to optimise local microstructural patterns, which are expressed as particle/pore distributions in a regular hexahedron-shaped unit box with the dimensions $40 \times 40 \times 40$ μm^3. Appropriate objective functions were defined to assess particle damage as independent mathematical parameters that were not experimentally measureable but were computable by employing 3D image-based numerical simulations. In addition, tens of design parameters were prepared, which quantitatively expressed the size, shape, and spatial distribution of Al_2Cu particles and pre-existing micro pores. The number of design parameters was reduced from 86 to 4 for each objective function during the two-step coarsening process. The surrogate model provided the size, shape, and spatial distribution of the particles and micro pores in the unit box as the weakest

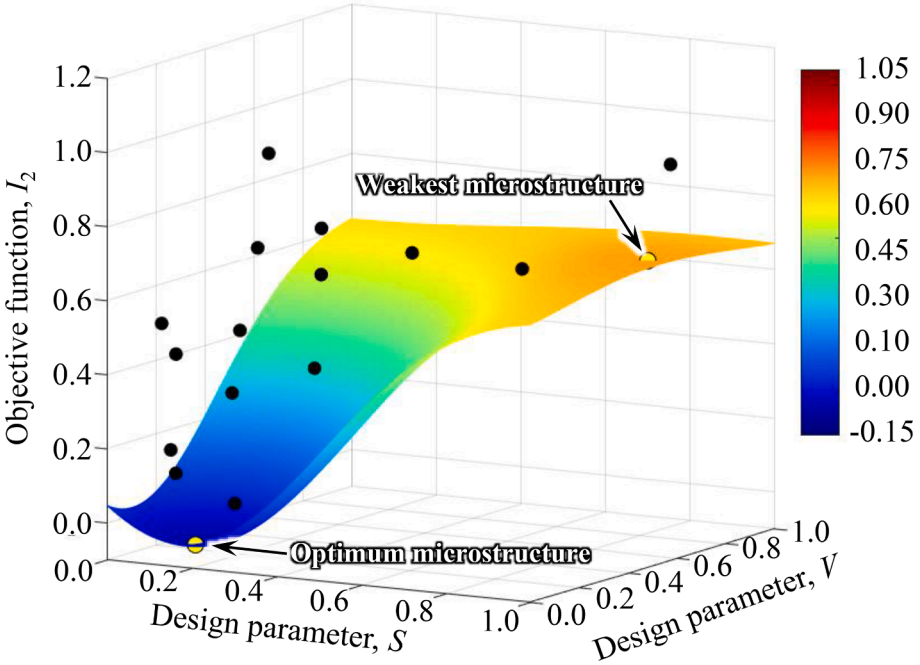

(a) Response surface of objective function I_2 as functions of the two design parameters on Al_2Cu particles

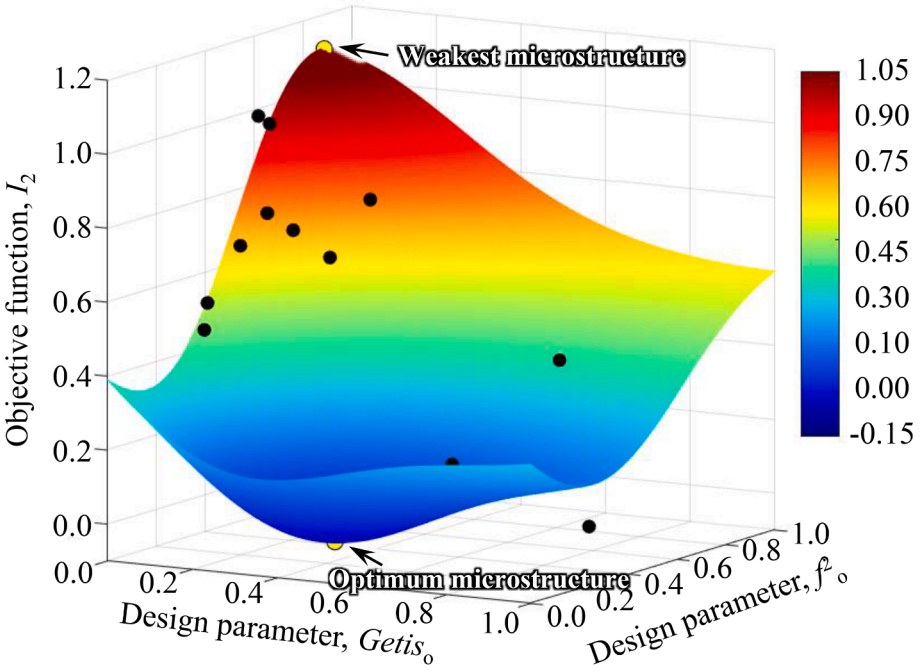

(b) Response surface of objective function I_2 as functions of the two design parameters on micro pores

Fig. 8. This shows the 3D response surfaces of objective function I_2, which were drawn as 3D contour maps. Two of the top four design parameters were selected to show a couple of 3D design spaces, with the remaining two parameters fixed at their average values in each figure.

and optimal (strongest) microstructural patterns together with their multi-dimensional distributions as forms of multi-dimensional response surfaces.

Half of the design parameters that survived through the coarsening process were associated with micro pores, especially the spatial distribution of pre-existing micro pores. This suggests the importance of pre-existing micro pores in relation to particle damage due to the enhancement of matrix plastic deformation and the elevation of stress triaxiality in the matrix. It was also clarified that the simple volume and surface area of particles are important parameters to describe particle damage through the elevation of particle stress and the equivalent plastic strain in the matrix. The response surface showed that the particles in optimised unit cells were relatively small with rather simple shapes and that micro pores exhibited rather moderate dispersion,

Table 1
This shows the predicted optimal values for the four selected design parameters for objective function I_2.

Design parameters	Optimum values to minimize I_2	
	Normalized values	Actual values
S*	0.162	25.0 μm^3
V**	0.0816	8.58 μm^3
f_o^{2***}	0.167	1.01
Getis$_o$****	0.384	0.278

* Surface area
** Volume
*** Aspect ratio
**** Getis's global statistics index.

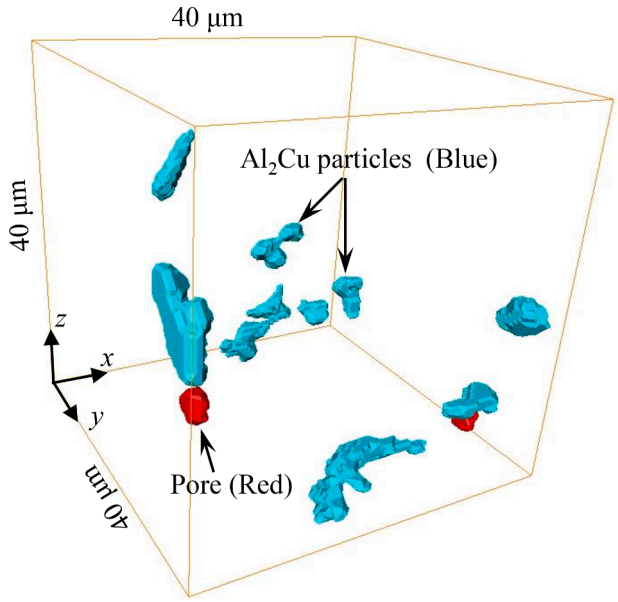

Fig. 9. This shows the 3D view of the local region (40 × 40 × 40 μm^3) that was sampled from the whole field of view so that the values of the four selected design parameters within the unit box were the closest to the optimal values shown in Table 1. Only micro pores and Al_2Cu particles are displayed, which are represented in red and light blue, respectively. (For interpretation of the references to colour in this figure legend, the reader is referred to the web version of this article.)

which implies that homogeneous particle/pore distributions are not necessarily the strongest. The optimised microstructural pattern in a unit cell was then visualised by sampling the local microstructural pattern that had design parameters closest to the optimal ones from the 3D image of an actual material specimen. Correlation coefficients between the selected design parameters for local microstructural patterns and particle damage were significantly higher than those for single-particle optimisation performed in the previous study.

Conventional research has taken the average of particle size and shape or other microstructural features and used this as an indicator for improving material properties. In the previous report [30] it was argued that material properties can be efficiently improved by knowing the best and worst values of particle properties, rather than the average values, and designing materials to reduce patterns close to the worst values and increase those close to the best values of the material structure. In the present paper we take this further and have considered that optimisation can be achieved by examining the microstructural patterns of local regions in the material, knowing their worst and best patterns, removing the worst local patterns from the microstructure and guiding them towards the best local patterns, taking into account the interference effects of the microstructures.

The methodology proposed in this paper enables presenting the weakest microstructural pattern and extracting the dominant factors from complex image-based data. It can provide new findings, insights, and reasonable interpretations of complex phenomena, leading to drastic improvements in the characteristics of materials through microstructural optimization. It is possible to move away from a conventional intuitive understanding of phenomena to a logical interpretation that is corroborated by the huge amounts of data. A 3D image-based numerical simulation utilises the particular microstructural features embedded in a single specimen, but in principle, it only leads to universal understanding after multiple repetitions. This is equivalent to testing a material multiple times. However, this is rarely realised due to the high computational costs. The methodology proposed in this paper compensates for such shortcomings and delivers the full potential of 3D image-based numerical simulations. By simply identifying a limited number of material design variables that are effective in controlling microstructure, and using them as indicators for limited and localised modification of the complex microstructure of real materials, significant improvements in macro-properties can be achieved. This is expected to lead to revolutionary improvements in the efficiency of materials design.

CRediT authorship contribution statement

Hiroyuki Toda: Writing – original draft, Visualization, Supervision, Project administration, Methodology, Funding acquisition, Data curation, Conceptualization. **Kyosuke Hirayama:** Writing – review & editing. **Han Li:** Visualization, Software, Methodology, Investigation, Formal analysis. **Rafael Batres:** Software, Methodology. **Seo Dowon:** Investigation, Formal analysis. **Hiro Fujihara:** Writing – review & editing.

Declaration of competing interest

The authors declare that they have no known competing financial interests or personal relationships that could have appeared to influence the work reported in this paper.

Data availability

Data will be made available on request.

Acknowledgements

The synchrotron experiments were performed with the approval of JASRI through the proposal numbers 2013B1027, 2020A1796, and 2020A1084. This work was supported by JSPS KAKENHI (grant numbers JP17H01328 and JP21H04624), the Japan Science and Technology Agency through the project Core Research for Evolutional Science and Technology (grant number JPMJCR1995), and the Light Metal Educational Foundation.

Appendix A. Supplementary data

Supplementary data to this article can be found online at https://doi.org/10.1016/j.commatsci.2024.113115.

References

[1] T. Kalil, C. Wadia, Materials Genome Initiative for Global Competitiveness (Whitepaper), National Science and Technology Council, Washington, DC, 2011.
[2] C. Yang, Y. Kim, S. Ryu, G.X. Gu, Prediction of composite microstructure stress-strain curves using convolutional neural networks, Mater. Des. 189 (2020) 108509.
[3] D.T. Fullwood, B.L. Adams, S.R. Kalidindi, A strong contrast homogenization formulation for multi-phase anisotropic materials, J. Mech. Phys. Solids 56 (2008) 2287–2297.
[4] Y. Wang, X. Hang, P. Damiano, Multiscale isogeometric topology optimization for lattice materials, Comput. Methods Appl. Mech. Eng. 316 (2017) 568–585.

[5] M. Fujioka, M. Shimoda, M. Al Ali, Shape optimization of periodic-microstructures for stiffness maximization of a macrostructure, Compos. Struct. 268 (2021) 113873.
[6] M. Seabra, J. Azevedo, A. Araújo, L. Reis, E. Pinto, N. Alves, R. Santos, J. P. Mortágua, Selective laser melting (SLM) and topology optimization for lighter aerospace components, Proc. Struct. Integr. 1 (2016) 289–296.
[7] W. Gebisa, H.G. Lemu, A case study on topology optimized design for additive manufacturing, IOP Conf. Series: Mater. Sci. Eng. 276 (2017) 012026.
[8] Y. Sun, W. Zeng, Y. Han, Y. Zhao, G. Wang, M.S. Dargusch, P. Guo, Modeling the correlation between microstructure and the properties of the Ti–6Al–4V alloy based on an artificial neural network, Mater. Sci. Eng. A 528 (2011) 8757–8764.
[9] H. Sheikh, S. Serajzadeh, Estimation of flow stress behavior of AA5083 using artificial neural networks with regard to dynamic strain ageing effect, J. Mater. Process. Technol. 196 (2008) 115–119.
[10] A. Bahrami, S.H. Mousavi Anijdan, A. Ekrami, Prediction of mechanical properties of DP steels using neural network model, J. Alloys Compd. 392 (2005) 177–182.
[11] M. Mahfouf, Optimal design of alloy steels using genetic algorithms, Advances in Computational Intelligence and Learning: Methods and Applications, Springer, Dordrecht, Netherland, 2002, pp. 425–436.
[12] R.C. Reed, Z. Zhu, A. Sato, D.J. Crudden, Isolation and testing of new single crystal superalloys using alloys-by-design method, Mater. Sci. Eng. A 667 (2016) 261–278.
[13] S. Pattanayak, S. Dey, S. Chatterjee, S.G. Chowdhury, S. Datta, Computational intelligence based designing of microalloyed pipeline steel, Comput. Mater. Sci. 104 (2015) 60–68.
[14] Y. Sun, W. Zeng, X. Ma, B. Xu, X. Liang, J. Zhang, A hybrid approach for processing parameters optimization of Ti-22Al-25Nb alloy during hot deformation using artificial neural network and genetic algorithm, Intermetallics 19 (2011) 1014–1019.
[15] R.G. Song, Q.Z. Zhang, Heat treatment optimization for 7175 aluminum alloy by genetic algorithm, Mater. Sci. Eng. C 17 (2001) 133–137.
[16] A. Li, H. Li, K. Li, Z. Gu, Applications of neural networks and genetic algorithms to CVI processes in carbon/carbon composites, Acta Mater. 52 (2004) 299–305.
[17] M.A. Groeber, M.A. Jackson, DREAM.3D: A digital representation environment for the analysis of microstructure in 3D, Integ. Mater. Manuf. Innov. 3 (2014) 56–72.
[18] F. Roters, P. Eisenlohr, C. Kords, D.D. Tjahjanto, M. Diehl, D. Raabe, DAMASK: the Düsseldorf advanced material simulation kit for studying crystal plasticity using an FE based or a spectral numerical solver, Proc. IUTAM: IUTAM Symposium Linking Scales Comput. 3 (2012) 3–10.
[19] M. Diehl, M. Groeber, C. Haase, D.A. Molodov, F. Roters, D. Raabe, Identifying structure–property relationships through DREAM.3D representative volume elements and DAMASK crystal plasticity simulations: An integrated computational materials engineering approach, JOM 69 (2017) 848–855.
[20] A. Raßloff, P. Schulz, R. Kühne, M. Ambati, I. Koch, A.T. Zeuner, M. Gude, M. Zimmermann, M. Kästner, Accessing pore microstructure–property relationships for additively manufactured materials, GAMM - Mitteilungen 44 (2021). ISSN: 0936-7195 Online ISSN: 1522-2608.
[21] L.M. Evans, E. Sözümert, B.E. Keenan, C.E. Wood, A. Plessis, A review of image-based simulation applications in high-value manufacturing, Arch. Computat. Methods Eng. 30 (2023) 1495–1522.
[22] K. Terada, T. Miura, N. Kikuch, Digital image-based modeling applied to the homogenization analysis of composite materials, Comput. Mech. 20 (1997) 331–346.
[23] H. Toda, M. Takata, T. Ohgaki, M. Kobayashi, T. Kobayashi, K. Uesugi, K. Makii, Y. Aruga, 3-D image-based mechanical simulation of aluminium foams: Effects of internal microstructure, Adv. Eng. Mater. 8 (2006) 459–467.
[24] L. Qian, H. Toda, K. Uesugi, M. Kobayashi, Direct observation and image-based simulation of three-dimensional tortuous crack evolution inside opaque materials, Phys. Rev. Lett. 100 (2008) 115505.
[25] H. Fujihara, H. Toda, K. Ebihara, M. Kobayashi, T. Mayama, K. Hirayama, K. Shimizu, A. Takeuchi, M. Uesugi, Assessment of hydrogen embrittlement behavior in Al-Zn-Mg alloy through multi-modal 3D image-based simulation, Int. J. Plast. 174 (2024) 103897.
[26] H. Toda, P.C. Qu, S. Ito, K. Shimizu, K. Uesugi, A. Takeuchi, Y. Suzuki, M. Kobayashi, Formation behaviour of blister in cast aluminium alloy, Int. J. Cast Met. Res. 27 (2014) 369–377.
[27] C.S. Chong, A.S. Kumar, H.P. Lee, Automatic mesh-healing technique for model repair and finite element model generation, Finite Elem. Anal. Des. 43 (2007) 1109–1119.
[28] M. Teranishi, O. Kuwazuru, M. Kobayashi, H. Toda, Statistical evaluation of fracture of inclusions in cast aluminum alloy by massively-parallel voxel finite element analysis and geometrical measurements, Trans. Jpn. Soc. Mechanic. Eng. 84 (2018) 18–00028.
[29] H. Toda, X-Ray CT, Hardware and Software Techniques, Springer Nature Singapore, Singapore, 2021.
[30] H. Toda, H. Li, R. Batres, K. Hirayama, H. Fujihara, Surrogate-based optimization of microstructural features of structural materials, Acta Mater. 257 (2023) 119188.
[31] J. Shawe-Taylor, S. Sun, A review of optimization methodologies in support vector machines, Neurocomputing 74 (2011) 3609–3618.
[32] C.C. Chang, C.J. Lin, LIBSVM, A library for support vector machines, ACM Trans. Intell. Syst. Technol. 2 (2011) 27:1–27:27.
[33] W. Ponweiser, T. Wagner, M. Vincze, Clustered multiple generalized expected improvement: A novel infill sampling criterion for surrogate models, 2008 IEEE Congress on Evolutionary Computation (IEEE World Congress on Computational Intelligence), Hong Kong, China, 2008, pp. 3515-3522.
[34] J. Segurado, C. Gonza´lez, J. Llorca, A numerical investigation of the effect of particle clustering on the mechanical properties of composites, Acta Mater. 51 (2003) 2355–2369.
[35] H. Toda, H. Oogo, K. Horikawa, K. Uesugi, A. Takeuchi, Y. Suzuki, M. Nakazawa, Y. Aoki, M. Kobayashi, The true origin of ductile fracture in aluminum alloys, Metall. Mater. Trans. A 45 (2014) 765–776.
[36] N.M. El Chazly, M.M. Farag, Inhomogeneity of plastic deformation and fracture modes in two-phase alloys, Mater. Sci. Eng. 55 (1982) 29–38.
[37] A. Hosokawa, H. Toda, R. Batres, H. Li, O. Kuwazuru, M. Kobayashi, H. Yakita, Ductile fracture via hydrogen pore mechanism in an aluminum alloy, Quantitative microstructural analysis and image-based finite element analysis, Mater. Sci. Eng. A 671 (2016) 96–106.
[38] F.A. Sadjadi, E.L. Hall, Three-dimensional moment invariants, IEEE Trans. Pattern Anal. Mach. Intell. 2 (1980) 127–136.
[39] G. Shakhnarovish, T. Darrell, P. Indyk, Nearest-Neighbor Methods in Learning and Vision, Neural Information Processing series, The MIT Press, 2006, ISBN 0-262-19547-X.
[40] P.J. Diggle, Statistical Analysis of Spatial and Spatio-Temporal Point Patterns, 3rd ed., Chapman and Hall/CRC Press, 2013.
[41] J. Mateu, J.L. Usó, F. Montes, The spatial pattern of a forest ecosystem, Ecol. Model. 108 (1998) 163–174.
[42] A.M. Rodrigues, J.A. Tenedorio, Sensitivity Analysis of Spatial Autocorrelation Using Distinct Geometrical Settings: Guidelines for the Urban Econometrician, 14th International Conference on Computational Science and Its Applications (ICCSA), 2014, pp. 345-356.
[43] R.C. Geary, The contiguity ratio and statistical mapping, Incorporated Statistician 5 (1954) 115–145.
[44] P.A.P. Moran, Notes on continuous stochastic phenomena, Biometrika 37 (1950) 17–23.
[45] A. Getis, J.K. Ord, The analysis of spatial association by use of distance statistics, Geogr. Anal. 24 (1992) 189–206.
[46] J.R. Rice, D.M. Tracey, On the ductile enlargement of voids in triaxial stress fields, J. Mech. Phys. Solids 17 (1969) 201–217.
[47] G.E.P. Box, K.B. Wilson, On the experimental attainment of optimum conditions, J. Royal Stat. Soc., Series B 13 (1951) 1–45.
[48] J. Evans, Straightforward statistics for the behavioral sciences, CA Brooks/Cole Publishing, Pacific Grove, 1996.
[49] D. Schneberk, N. Shashishekhar, High-speed CT imaging for today's industry, Non-Destructive Testing Condition Monitoring 50 (2008) 19–21.
[50] H. Toda, K. Hirayama, S. Yamaguchi, H. Fujihara, R. Higa, K. Shimizu, A. Takeuchi, M. Uesugi, Dominant factors controlling the initiation of hydrogen embrittlement in Al–Zn–Mg alloy, Mater. Trans. 64 (2023) 2729–2738, https://doi.org/10.2320/matertrans.MT-M2023116.
[51] H. Toda, H. Fujihara, K. Hirayama, K. Shimizu, A. Takeuchi, M. Uesugi, Hydrogen induced debonding of Mg_2Si particle / aluminum interface in Al-Mg-Si alloy, Mater. Trans. (2024), https://doi.org/10.2320/matertrans.MT-M2024026.
[52] H. Toda, S. Feng, H. Fujihara, A. Takeuchi, M. Uesugi, Assessment of fatigue crack initiation behaviour in Ti-6Al-4V alloy Using a coarsened surrogate model, Mater. Sci, Eng. A (2024) under review.